EPJ Appl. Metamat. **8**, 12 (2021)

https://doi.org/10.1051/epjam/2021004

EPJ Applied Metamaterials

Available online at:
epjam.edp-open.org

Metamaterial Research Updates from China

RESEARCH ARTICLE OPEN ACCESS

Dual-band beam steering THz antenna using active frequency selective surface based on graphene

Yao-Jia Yang, Bian Wu*, Yu-Tong Zhao, and Chi-Fan

National Key Laboratory of Antennas and Microwave Technology, Key Laboratory of Millimeter Wave and Terahertz Technology, Xi'an 710071, PR China

Received: 12 January 2021 / Accepted: 14 March 2021

Abstract. A dual-band independently beam steering THz antenna is presented, which is composed of a broadband omnidirectional monopole source antenna surrounded by six hexagonal active frequency selective surface (AFSS) screens with switchable filtering response in two bands. By controlling the chemical potential from 0 eV to 0.5 eV, the AFSS screen can achieve the conversion between high transmission (ON state) and almost total reflection (OFF state) at two frequency ranges independently. Therefore, the radiation beams of the THz antenna in two bands can be steered from 360° large angle scanning and omnidirectional radiation with flexible combinations.

Keywords: Graphene / frequency selective surface / beam steering antenna / THz antenna

The pattern reconfigurable antenna has been widely exploited because it not only improves the system capacity and anti-interference ability, but also reduces the physical volume and system complexity. Phased array antenna is the traditional method to implement this technology, however, the complex feed networks make the antenna system bulky and expensive [1–3]. Frequency selective surface (FSS) is a periodic structure capable of transmitting or reflecting EM waves at resonance [4]. In recent years, active frequency selective surfaces [5] have been widely used in the beam steering antennas [6,7]. However, since most of the tunable components has problems to be used in the terahertz frequency ranges, many new materials [8] and technologies are applied to THz beam scanning antennas [9–12].

As a two-dimensional carbon material [13], graphene has the unique property that its complex surface conductivity depends on the carrier density and can be controlled by gate voltage [14], which makes it a novel tunable material suitable for the reconfigurable device design. Therefore, many graphene-based tunable THz devices such as active frequency selective surface (AFSS) [15], modulator [16], sensor [17,18], polarization selective surfaces [19], tunable absorber [20–23] and reconfigurable antenna [24,25] have been proposed. In the previous work, we have demonstrated a large angle beam steering THz antenna using active frequency selective surface based on hybrid graphene-gold structure [26].

However, most of the traditional AFSS-based pattern reconfigurable antennas can only dynamically change the radiation pattern in a single band. In the multifunctional THz communication system, the dual-frequency beam steering antenna becomes important. Recently, some dual-band beam sweeping antennas in gigahertz [6,7] are proposed, but it utilizes band-stop FSS or cannot control independently, which is not suitable for practical application. Until now, as far as we know, it is still a challenge to achieve dual-band independently controllable pattern reconfigurable antennas in the terahertz regime.

In this paper, we present a dual-band beam steering THz antenna with flexible beam radiations using graphene-based AFSS. The antenna consists of a broadband monopole terahertz source antenna placed in the center of a hexagonal switchable AFSS screen. By changing the bias voltages of different parts of the hexagon AFSS screen, both beam steering and omnidirectional radiation patterns could be obtained to cover the entire azimuth plane of the antenna at both frequencies.

The geometry of the proposed dual-band switchable AFSS unit cell is shown in Figure 1a. Each AFSS unit cell consists of four layers: gold pattern layer, p-type doped silicon layer, silicon dioxide layer and graphene pattern layer. The silicon dioxide layer is chosen as insulating layer between p-type silicon and the graphene patches. The relative dielectric constant of p-type silicon and silicon dioxide is 11.7 and 4, respectively. As shown in Figure 1b, the designed FSS based on the cross-shaped slot in the center and the quarter folded slot rings in the four corners produces two different resonances. The cross-shaped slot is adopted here due to its simple structure and stable

* e-mail: bwu@mail.xidian.edu.cn

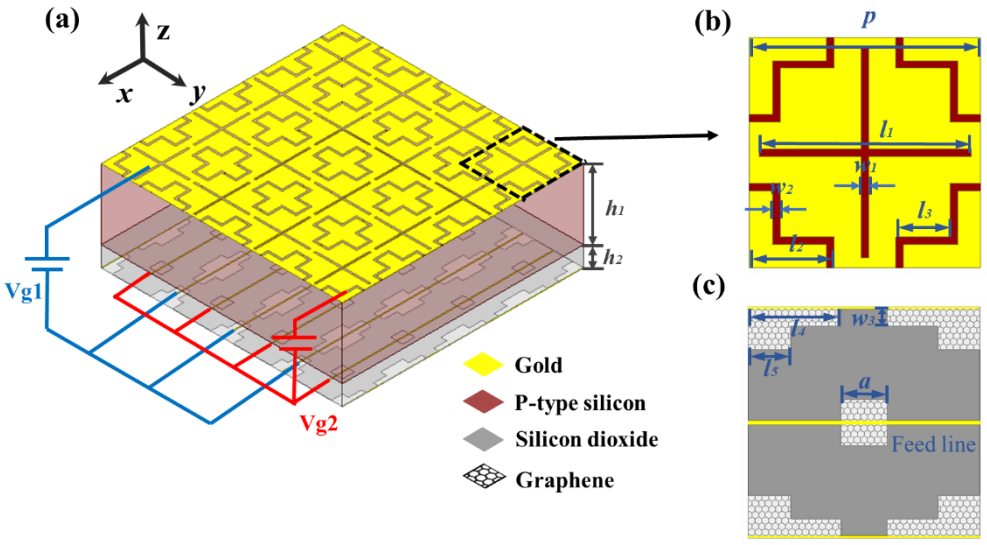

Fig. 1. Schematic diagram of (a) 3D view, (b) top view, and (c) bottom view of the proposed AFSS unit cell. The relevant geometrical dimensions are p = 60, $l_1 = 55$, $l_2 = 22$, $l_3 = 16$, $l_4 = 24$, $l_5 = 11$, $w_1 = 2$, $w_2 = 2$, $w_3 = 5$, a = 12, all in μm. The thicknesses of the p-type doped silicon, silicon dioxide substrates are $h_1 = 3$ μm, $h_2 = 0.3$ μm, respectively.

characteristic. To achieve separate feeding of different graphene patches, we propose a new graphene loading method as shown in Figure 1c, the square graphene patch is loaded under the cross-shaped slot, and quarter cross-shaped graphene patches are loaded under the quarter folded slot rings, respectively. Two kinds of bias voltages are applied between the gold pattern layer (DC connected with the p-type silicon layer) and the graphene pattern layer, thus controlling the chemical potentials as well as the surface conductivities of graphene patches. By tuning the two bias voltages separately on the two shapes of graphene patches, the transmission and reflection characteristics of the two passbands can be adjusted independently.

The complex surface conductivity $\sigma(\omega, \mu_c, \Gamma, T)$ of monolayer graphene can be derived from the Kubo formula which includes interband and intraband contributions [27,28]

$$\sigma_{intra} \approx \frac{-je^2 k_B T}{\pi\hbar(\omega - j2\Gamma)}\left[\frac{\mu_c}{k_B T} + 2\ln\left(e^{-\mu_c/(k_B T)} + 1\right)\right] \quad (1)$$

$$\sigma_{inter} \approx \frac{-je^2}{4\pi\hbar}\ln\left(\frac{2|\mu_c| - (\omega - j2\Gamma)\hbar}{2|\mu_c| + (\omega - j2\Gamma)\hbar}\right) \quad (2)$$

where ω is the operating angular frequency, μ_c is chemical potential, e is the charge of an electron, k_B is the Boltzmann constant, $\hbar$ is the reduced Planck constant, $\Gamma = 1/(2\tau)$ represents the scattering rate and τ is the relaxation time, T is the temperature in Kelvin. Based on a theoretical estimation of the maximum mobility in graphene, we assume $T = 300$ K and $\tau = 100$ fs [29]. The chemical potential μ_c can be tuned by applying a transverse electric field via a DC biased gating structure [30], it can be approximately expressed as

$$\mu_c \approx \hbar v_f \sqrt{\frac{\pi\varepsilon_r\varepsilon_0 V_{dc}}{e t_s}} \quad (3)$$

where ε_r and ε_0 are the permittivity of substrates and vacuum respectively, V_{dc} is the bias voltage, $v_f = 1.1 \times 10^6$ m/s is the Fermi velocity in graphene. According to formula (3), it can be calculated that the voltage required to adjust the graphene chemical potential from 0 to 0.5 eV is 50 V. This has been proven achievable in previous research [31].

The AFSS is a periodic structure which can be analyzed by the EM simulation softwave ANSYS HFSS. The graphene patches can be modeled as the impedance boundary with the complex impedance as $Zs = 1/\sigma$. Figure 2 shows the current distributions at $f_1 = 0.96$ THz and $f_2 = 1.21$ THz under different chemical potentials. It can be seen from Figure 2a that when $\mu_{c1} = 0$ eV, $\mu_{c2} = 0.5$ eV, f_1 is generated by the resonance of quarter folded slot rings with strong current density at the four corners and the resonance at f_2 is significantly reduced due to the loss of graphene. As shown in Figure 2b, when $\mu_{c1} = 0.5$ eV, $\mu_{c2} = 0$ eV, f_2 is generated by the resonance of cross-shaped slot with large current density at the slot end and the resonance at f_1 is significantly reduced due to the loss of quarter cross-shaped graphene patches. There is almost no interaction between the two frequencies.

The voltages V_{g1} and V_{g2} control the chemical potentials μ_{c1} of the cross-shaped graphene patch and μ_{c2} of the square graphene patch, respectively. Figure 3a shows the simulated transmission coefficient with μ_{c1} changes from 0 to 0.5 eV and μ_{c2} keeps 0 eV, while Figure 3b shows the simulated transmission coefficient as μ_{c1} remains 0 eV and μ_{c2} varies from 0 to 0.5 eV. It can be seen that μ_{c1} controls the transmission amplitude at $f_1 = 0.96$ THz while μ_{c2} dynamically tunes the transmission amplitude at $f_2 = 1.21$ THz. In this way, the proposed AFSS can achieve the conversion between high transmission (ON state) and large reflection (OFF state) at two frequency bands independently. For simplicity, here we use the 2-bit code with the first code to represent the state of f_1 and the

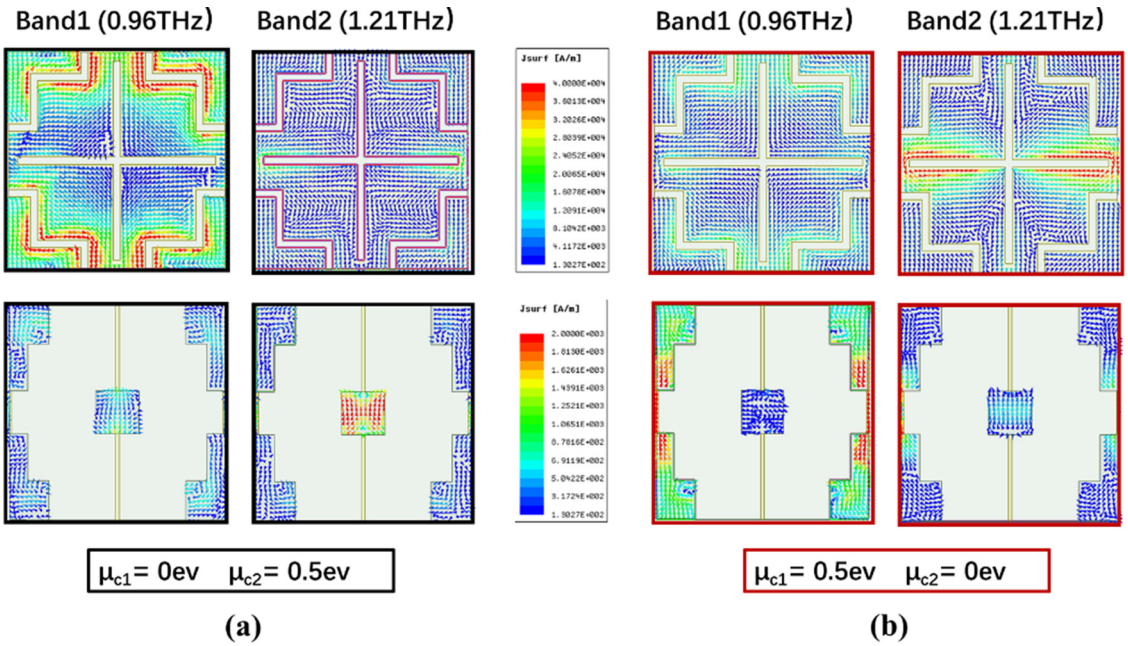

Fig. 2. Surface current distribution of AFSS in different states at frequencies $f_1 = 0.96$ THz and $f_2 = 1.21$ THz, respectively.

second code to represent the state of f_2, 0 for the ON state and 1 for the OFF state. Figure 3c and d show the reflection and transmission coefficients in the four coded states of 00, 01, 10 and 11, respectively. In the "00" state, the transmission coefficient is −1.5 dB at 0.96 THz and −1.3 dB at 1.21 THz, indicating high transmission (ON) states appear in two bands. In the "01" state, the transmission state at 0.96 THz is basically unchanged, while the transmission coefficient is −10.8 dB at 1.21 THz, which means the second band switches to OFF state. In the "10" state, the first band switches to OFF state while the second band remains ON state. In the "11" state, both bands switch to OFF states. The robustness of changing the incident angle of the incidence plane wave under TE polarization is studied. As shown in Figure 3e and f, the two transmission bands remain stable with the increased incident angle.

As shown in Figure 4a, a broadband omnidirectional monopole antenna is designed as a radiating source and surrounded by a hexagonal AFSS screen. Each side of the hexagonal AFSS screen is composed of a 2×4 AFSS array with the unit cell structure described above. And the gold line structure is designed to apply DC voltage. Figure 4b shows the structure of the broadband monopole source antenna, which is composed of an inverted trapezoid element as a main resonator and a small ground plane on the bottom of the substrate. This monopole antenna is constructed on Rogers RO4350B substrate with a relative dielectric constant of 3.66. It is selected here for its simple structure and ability to provide an omnidirectional radiation pattern in the azimuth plane at both 0.96 and 1.21 THz, as shown in Figure 4d. As shown in Figure 4c, this monopole antenna has a wide bandwidth covering 0.9–1.4 THz. After adding a hexagonal AFSS screen with filtering characteristics, and by controlling the four coded states of AFSS, four corresponding antenna states can be obtained. In the "00" state, two narrow operating bands are obtained. In the "01" state, the first band remains operating and the second band switches OFF state. In the "10" state, the first band switches OFF state and the second band remains operating. In the "11" state, both bands switch to OFF states.

As illustrated in Figure 5, four typical operating states are analyzed in order to verify the proposed THz antenna can realize beam sweeping at two frequencies independently. For the convenience of explanation, AFSS in each side is abstracted to black border rectangles numbered 1–6 represent the cross-shaped graphene patch operating at 0.96 THz and red border rectangles numbered 7–12 represent the square graphene patch works at 1.21 THz. The yellow color means ON state and blue color indicates OFF state, which can be adjusted by the bias voltages of each side independently. The feeding method of each face is shown in Figure 4a.

Case I: As shown in Figure 5a, for the cross-shaped graphene patches numbered 1–6, three adjacent sides are switched to OFF state at 0.96 THz, and the others are switched to ON state. For the rectangular graphene patches numbered 7–12, all sides of the AFSS are switched to ON state at 1.21 THz. As shown in Figure 5e and f, the radiation pattern has the ability to scan the entire azimuth plane in six steps at 0.96 THz. Meanwhile, it remain omnidirectional as the monopole antenna at 1.21 THz.

Case II: As shown in Figure 5b, for the cross-shaped graphene patches of 1–6, all sides of the AFSS are switched to ON state at 0.96 THz. For the square graphene patches numbered 7–12, three adjacent sides are switched to OFF state at 1.21 THz, and the others are switched to ON state. The radiation patterns at 1.21 THz realize 360° beam steering in six steps as shown in Figure 5h. Figure 5g

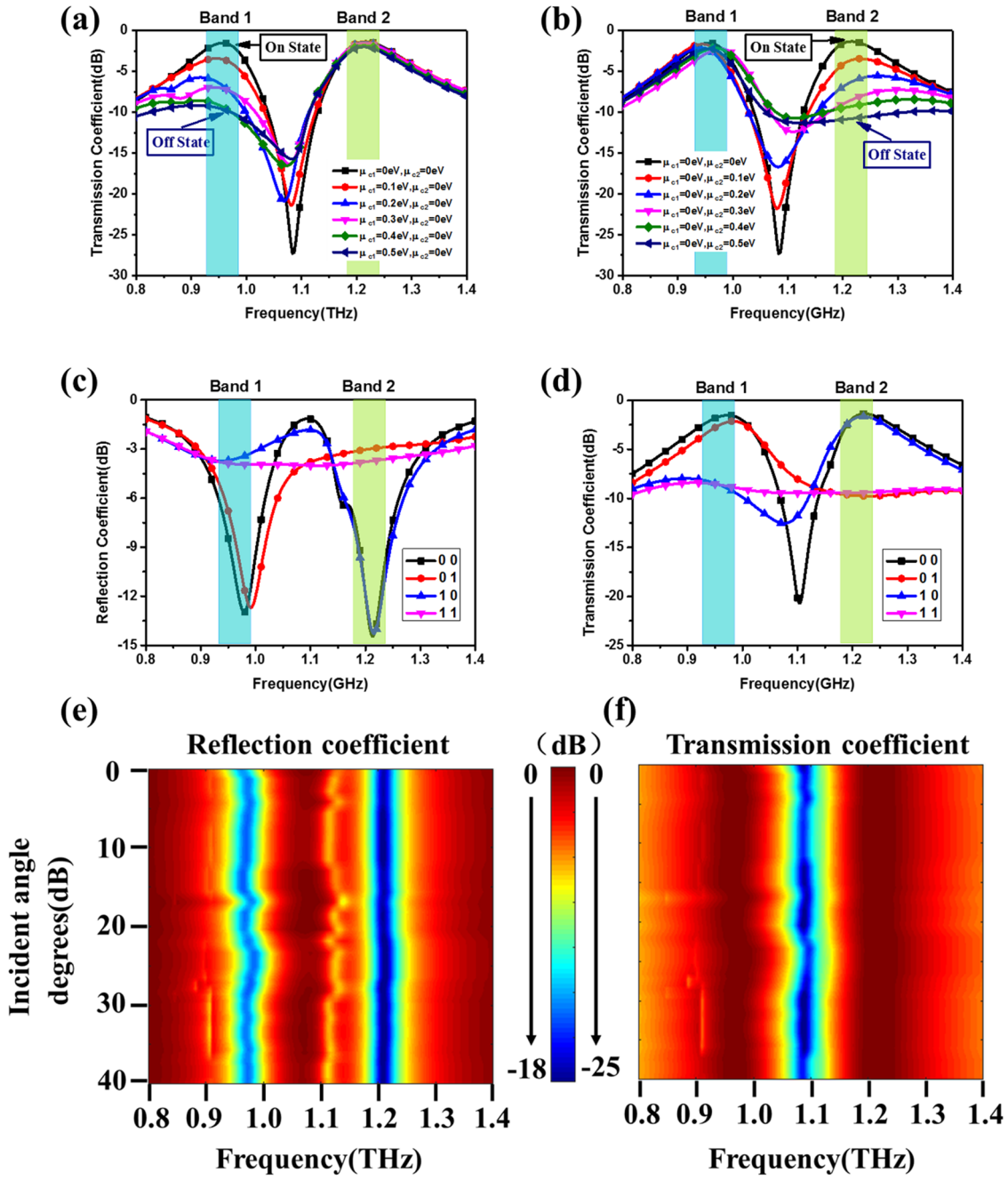

Fig. 3. The transmission or reflection spectra of the AFSS unit cell. (a) Transmission with various μ_{c1} and fixed μ_{c2}. (b) Transmission with various μ_{c2} and fixed μ_{c1}. (c) Reflection in four coded states. (d) Transmission in four coded states. (e) The reflection and (f) transmission spectra with various incident angles from 0° to 40° for TE polarizations.

shows the stable omnidirectional radiation patterns at 0.96 THz.

Case III: As shown in Figure 5c, for both the graphene patches 1–6 and 7–12, three adjacent sides are switched to OFF state and the others are switched to ON state. The radiation patterns shown in Figure 5i has the ability to scan the entire azimuth plane in six steps at both 0.96 and 1.21 THz simultaneously.

Case IV: As shown in Figure 5d, for both the graphene patches numbered 1–6 and 7–12, the OFF state of the AFSS on each side is different between every two adjacent faces. For example, when the number 2-4-6 and 7-9-11 are on OFF state, and the number 1-3-5 and 8-10-12 are switched to ON state, the antenna can radiate in three different directions as shown in Figure 5j at two frequencies simultaneously.

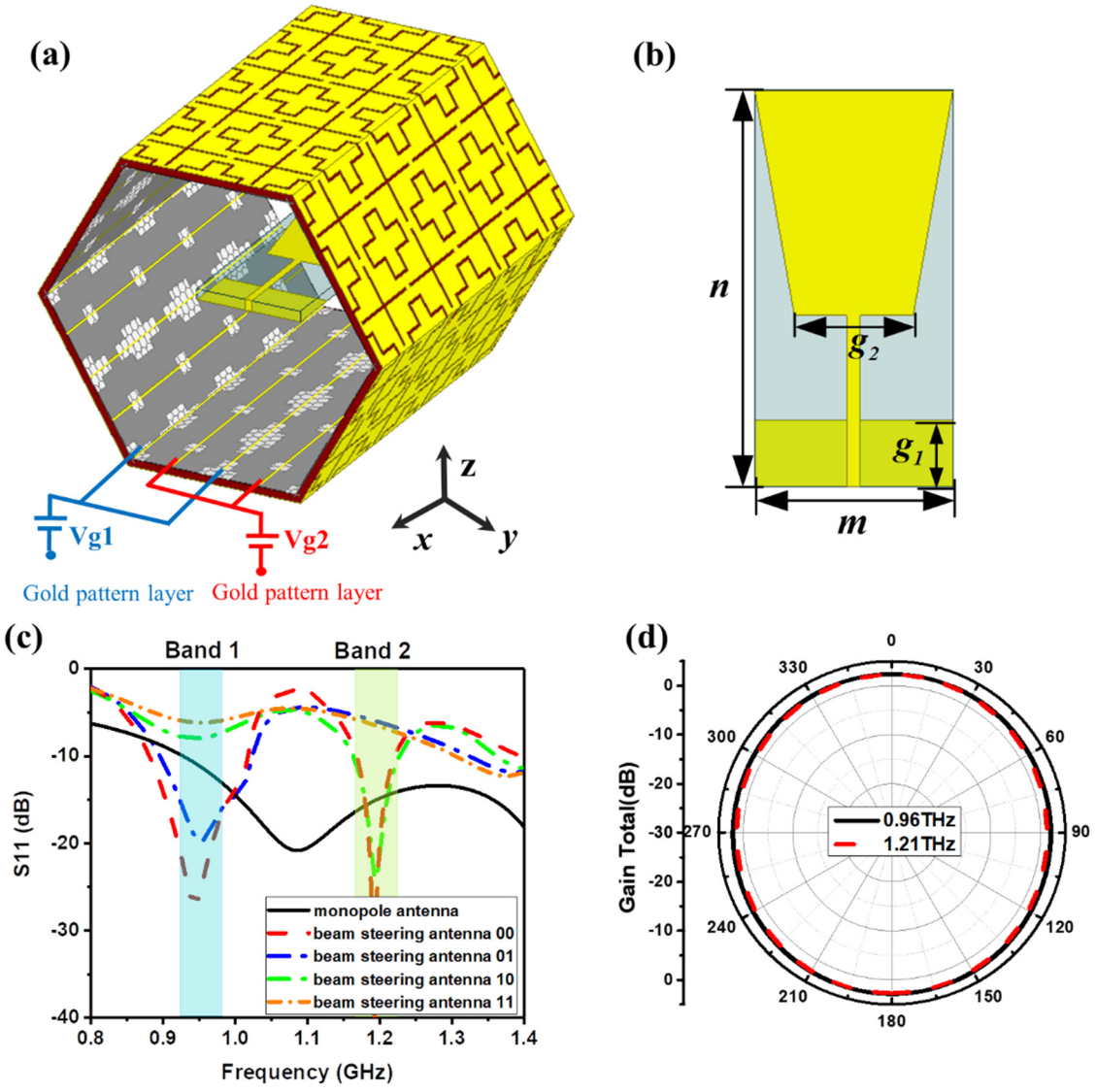

Fig. 4. (a) 3D view of the proposed dual-band beam steering THz antenna. (b) Geometry of the broadband omnidirectional monopole source antenna. The relevant geometrical dimensions are $m = 72$, $n = 144$, $g_1 = 33.6$, $g_2 = 43.2$, all in μm. (c) Reflection coefficients of the broadband omnidirectional source antenna and the dual-band beam steering THz antenna under different states. (d) Radiation patterns of the omnidirectional source antenna on the horizontal plane at two frequencies.

An open question that remains to be answered is the practical realization of the structures we propose here. Fortunately, recent advances in the fabrication of graphene [32–34] let us be optimistic about the feasibility of such structures in the near future. Additionally, biasing graphene seems difficult in practice. One can use self-biased graphene layers [35] connected to opposite poles of a voltage source. Finally, if bias voltage should be avoided, graphene layers can be excited optically [36,37].

In conclusion, a dual-band beam sweeping THz antenna is achieved by loading a hexagonal AFSS screen around a broadband omnidirectional monopole antenna. The graphene-based AFSS unit cell consists of aperture-type frequency selective surface loading graphene patches. By applying bias voltages separately to the two kinds of graphene patches, the transmission property in the two bands can be adjusted independently. Four typical cases of the antenna with six sides of the AFSS screen operating at ON/OFF state in two bands are demonstrated to validate the antenna can achieve beam sweeping in the entire azimuth plane with six steps and omnidirectional pattern at 0.96 and 1.21 THz simultaneously. This multifunctional THz antenna is promising for large angle beam scanning in terahertz multiband systems.

The authors would like to acknowledge support from the National Natural Science Foundation of China (Grant No. 61771360, U19A2055, 62071357), the key Industry chain Project of Shaanxi Province (Grant No. 2018ZDCXL-GY-08-03-01), the Fundamental Research Funds for the Central Universities, the Innovation Fund of Xidian University.

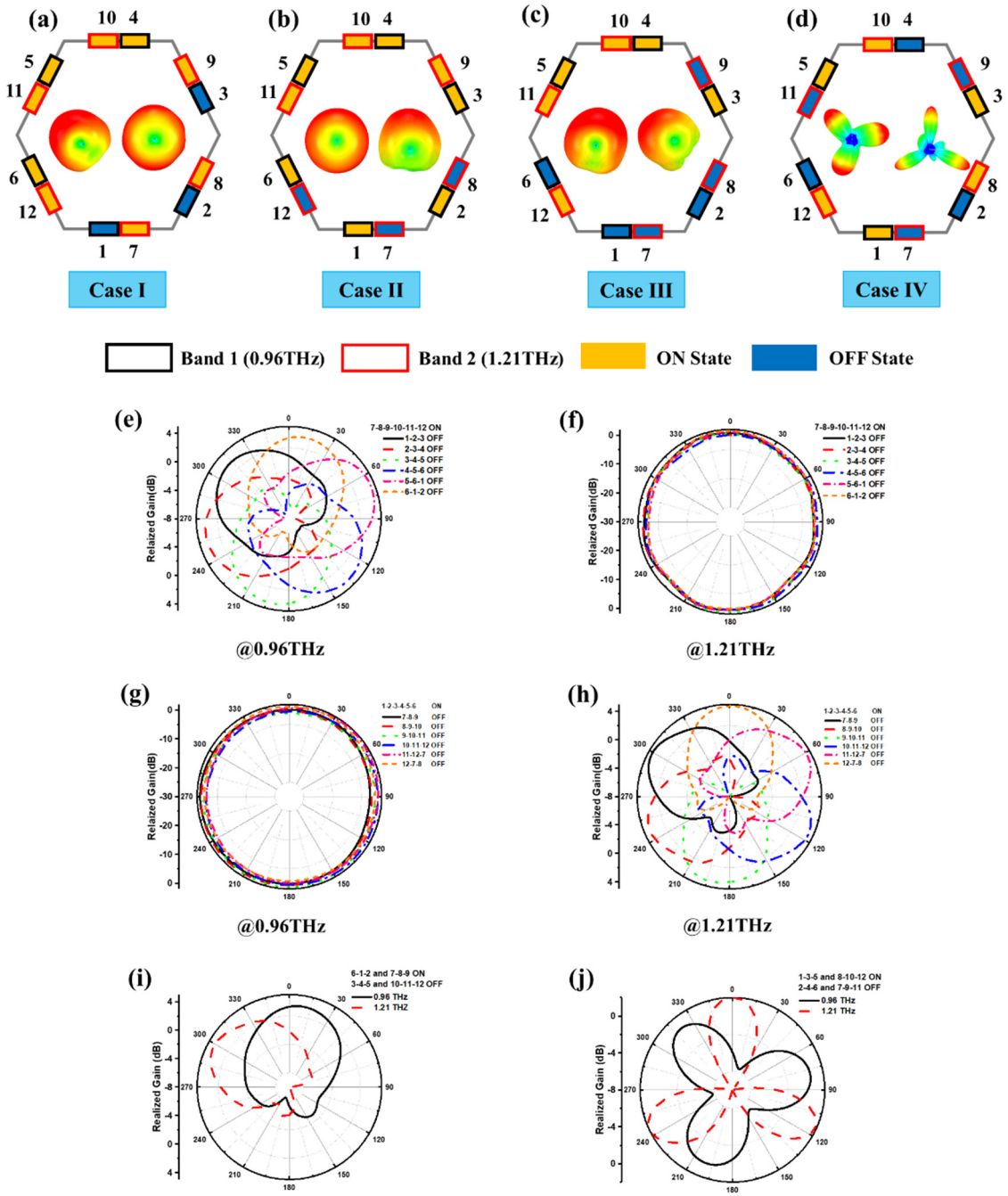

Fig. 5. Topologies of the beam steering antenna under different ON/OFF states. (a) Case I, (b) Case II, (c) Case III and (d) Case IV. Radiation patterns in the azimuth plane of (be Case I at 0.96 THz, (f) Case I at 1.21 THz, (g) Case II at 1.21 THz, (h) Case II at 0.96 THz, (i) Case III at two frequencies, and (j) Case IV at two frequencies.

References

1. V.S. Rao, V.V. Srinivasan, S. Pal, Electron. Lett. **45**, 441 (2009)
2. W. Zhou, M. Stead, S. Weiss et al., Appl. Opt. **56**, B5 (2016)
3. T. Tatoli, D. Conteduca et al., Appl. Opt. **55**, 4342 (2016)
4. T.K. Wu, Frequency Selective Surface and Grid Array (Wiley, New York, 1995)
5. P.S. Taylor, E.A. Parker, J.C. Batchelor, IEEE Trans. Antennas Propag. **59**, 3265 (2011)
6. J. Li, Q. Zeng, R. Liu, T.A. Denidni, IEEE Trans. Antennas Propag. **65**, 1542 (2017)
7. C. Gu, B.S. Izquierdo, S. Gao, J.C. Batchelor, E.A. Parker et al., IEEE Trans. Antennas Propag. **65**, 1393 (2017)
8. R. Ozaki, K. Kihara, K. Matsuura, K. Kadowaki, T.Q. Duong, H. Moritake, Appl. Phys. Express **13**, 051003 (2020)

9. T.P. Steinbusch, H.K. Tyagi, M.C. Schaafsma, G. Georgiou, J.G. Rivas, Opt. Express **22**, 26559 (2014)
10. B. Orazbayev, M. Beruete, I. Khromova, Opt. Express **24**, 8848 (2016)
11. B. Ratni, J. Yi, X. Ding, A. Lustrac et al., Opt. Express **26**, 6724 (2018)
12. H. Kim, M. Kim, Opt. Express **28**, 16822 (2020)
13. A.K. Geim, Science **324**, 1530 (2009)
14. A. Vakil, N. Engheta, Science **332**, 1291 (2011)
15. Y. Zhang, Y. Feng, B. Zhu et al., Opt. Express **22**, 22743 (2014)
16. B. Huang, W. Lu, Z. Liu, S. Gao, Opt. Express **26**, 7358 (2018)
17. R. Wang, Z. Ren, D. Kong, H. Wu, B. Hu, Z. He, Appl. Phys. Express **13**, 067001 (2020)
18. Y.P. Gu, X.T. Pu, H. Zhong, J. Chen, C.J. Tang, Z. Yu, Appl. Phys. Express **13**, 022013 (2020)
19. Y. Li, J. Zhao, H. Lin, W. Milne, Y. Hao, Opt. Express **23**, 7227 (2015)
20. Y.T. Zhao, B. Wu, B.J. Huang, Q. Cheng, Opt. Express **25**, 7161 (2017)
21. Y.M. Qing, H.F. Ma, T.J. Cui, ACS Photonics **6**, 2884 (2019)
22. Y.M. Qing, H.F. Ma, T.J. Cui, Carbon **145**, 596 (2019)
23. Y.M. Qing, H.F. Ma, Y.Z. Ren, S. Yu, T.J. Cui, Opt. Express **27**, 5253 (2019)
24. C.L. Wang, Y.Q. Wang, H. Hu, D.J. Liu, D.L. Gao, L. Gao, Opt. Express **27**, 35925 (2019)
25. M. Qu, M. Rao, S. Li, D. Li, AIP Adv. **7**, 095307 (2017)
26. B. Wu, Y. Hu, Y.T. Zhao, W.B. Lu, W. Zhang, Opt. Express **26**, 15353 (2018)
27. V.P. Gusynin, S.G. Sharapov, J.P. Carbotte, J. Phys.: Condens. Matter **19**, 026222 (2007)
28. G.W. Hanson, J. Appl. Phys. **103**, 064302 (2008)
29. F. Valmorra, G. Scalari, C. Maissen, Nano Lett. **13**, 3193 (2013)
30. J.S. Gómez-Díaz, J. Perruisseau-Carrier, Opt. Express **21**, 15490 (2013)
31. B. Sensale-Rodriguez, R. Yan, M.M. Kelly et al., Nat. Commun. **3**, 780 (2012)
32. B. Wu, H.M. Tuncer, M. Naeem, B. Yang, M.T. Cole, W.I. Milne, Y. Hao, Sci. Rep. **4**, 4130 (2015)
33. H. Chen, W. Lu, Z. Liu, J. Zhang, A. Zhang, B. Wu, IEEE Trans. Microw. Theory Technol. **66**, 3807 (2018)
34. H. Murata, K. Nozawa, N. Saitoh, N. Yoshizawa, T. Suemasu, K. Toko, Appl. Phys. Express **13**, 055502 (2020)
35. J.S. Gomez-Diaz, C. Moldovan, S. Capdevila, J. Romeu, L.S. Bernard, A. Magrez, A.M. Ionescu, J. Perruisseau-Carrier, Nat. Commun. **6**, 6334 (2015)
36. J. Chen, M. Badioli, P. Alonso-González, S. Thongrattanasiri, F. Huth, J. Osmond, M. Spasenović, A. Centeno, A. Pesquera, P. Godignon, A.Z. Elorza, N. Camara, F.J. García de Abajo, R. Hillenbrand, F.H.L. Koppens, Nature **487**, 77 (2012)
37. L. Yang, C. Pei, A. Shen, C. Zhao, Y. Li, X. Li, H. Yu, Y. Li, X. Jiang, J. Yang, Sci. Rep. **5**, 9206 (2015)

Cite this article as: Yao-Jia Yang, Bian Wu, Yu-Tong Zhao, Chi-Fan, Dual-band beam steering THz antenna using active frequency selective surface based on graphene, EPJ Appl. Metamat. **8**, 12 (2021)